OSSOS. XXI. Collision Probabilities in the Edgeworth–Kuiper Belt

Abedin Y. Abedin[1] , J. J. Kavelaars[1] , Sarah Greenstreet[2,3] , Jean-Marc Petit[4] , Brett Gladman[5] , Samantha Lawler[6] ,
Michele Bannister[7], Mike Alexandersen[8] , Ying-Tung Chen[9] , Stephen Gwyn[1], and Kathryn Volk[10]

[1] National Research Council of Canada, Herzberg Astronomy and Astrophysics, 5071 West Saanich Road, Victoria, BC V9E 2E7, Canada;
abedin.abedin@nrc-cnrc.gc.ca
[2] B612 Asteroid Institute, 20 Sunnyside Avenue, Suite 427, Mill Valley, CA 94941, USA
[3] DIRAC Center, Department of Astronomy, University of Washington, 3910 15th Avenue NE, Seattle, WA 98195, USA
[4] Institut UTINAM, CNRS-UMR 6213, Université Bourgogne Franche Comté BP 1615, F-25010 Besançon Cedex, France
[5] Department of Physics and Astronomy, 6224 Agricultural Road, University of British Columbia, Vancouver, BC, Canada
[6] Campion College and the Department of Physics, University of Regina, Regina, SK S4S 0A2, Canada
[7] University of Canterbury, Christchurch, New Zealand
[8] Minor Planet Center, Smithsonian Astrophysical Observatory, 60 Garden Street, Cambridge, MA 02138, USA
[9] Academia Sinica Institute of Astronomy and Astrophysics, Taiwan
[10] Lunar and Planetary Laboratory, University of Arizona: Tucson, AZ, USA
Received 2020 December 16; revised 2021 January 25; accepted 2021 January 27; published 2021 March 25

Abstract

Here, we present results on the intrinsic collision probabilities, P_I, and range of collision speeds, V_I, as a function of the heliocentric distance, r, in the trans-Neptunian region. The collision speed is one of the parameters that serves as a proxy for a collisional outcome (e.g., disruption and scattering of fragments, or formation of a crater, as both processes are related to the impact energy). We utilize an improved and debiased model of the trans-Neptunian object (TNO) region from the "Outer Solar System Origins Survey" (OSSOS). It provides a well-defined model of TNO orbital distribution, based on multiple opposition observations of more than 1000 bodies. We compute collisional probabilities for the OSSOS models of the main classical, resonant, detached+outer, and scattering TNO populations. The intrinsic collision probabilities and collision speeds are computed using Öpik's approach, as revised and modified by Wetherill for noncircular and inclined orbits. The calculations are carried out for each of the dynamical TNO groups, allowing for inter-population collisions as well as collisions within each TNO population, resulting in 28 combinations in total. Our results indicate that collisions in the trans-Neptunian region are possible over a wide range in (r, V_I) phase space. Although collisions are calculated to happen within $r \sim 20$–200 au and $V_I \sim 0.1$ km s^{-1} to as high as $V_I \sim 9$ km s^{-1}, most of the collisions are likely to happen at low relative velocities $V_I < 1$ km s^{-1} and are dominated by the main classical belt.

Unified Astronomy Thesaurus concepts: Trans-Neptunian objects (1705); Collision processes (2065)

Supporting material: tar.gz file

1. Introduction

The Edgeworth–Kuiper Belt (Kuiper Belt hereafter) is a torus-shaped agglomeration of small icy objects encircling the solar system. Extending from the orbit of Neptune at 30 au to more than 200 au from the Sun, the Kuiper Belt consists of more than $\sim 10^5$ trans-Neptunian objects (TNOs) with size $D > 100$ km (Petit et al. 2011). TNOs can be considered to consist of pristine building blocks, left over from solar system formation; they are unlikely to have been exposed to temperatures of $T > 50$ K (e.g., Jewitt & Luu 2004) over the age of the solar system.

Collisions between bodies inevitably lead to ejecta, regardless of whether the impact is disruptive or crater-forming, with the total mass and velocity distribution of liberated material being dictated by the energy of the impact (e.g., Melosh 1989; Fujiwara et al. 1989; Housen & Holsapple 1990; Benz & Asphaug 1999; Holsapple et al. 2002). The ejecta size distribution generally follows some power law, ranging from large boulders to dust particles, with the number of released fragments being inversely proportional to particle size. Understanding the impact velocity distribution and probability will aid in understanding the impact environment of these bodies and the expected rate of dust/debris production. These impacts may very well be responsible for the formation of dust rings and satellites around planets (Harris & Rings 1984; Charnoz

et al. 2009, 2018), and dusty exospheres around small bodies (e.g., Szalay et al. 2018); they may also serve as source and replenishment of the interplanetary dust flux (e.g., Kuchner & Stark 2010; Vitense et al. 2012; Poppe 2016) or lead to planetary surface cratering (e.g., Greenstreet et al. 2015, 2019). In particular, dust is dynamically short-lived and collisions provide an avenue to refresh that content.

Owing to the fundamental importance of the collisional processing for understanding the Kuiper Belt and the outer solar system, a number of early estimates of the collisional environment were made with only the slimmest of observational data to ground them. Stern (1995) argued that TNOs smaller than ~ 10 km are collisionally evolved, based on collision rate estimation between 35 and 70 au, while objects with radii $r > 100$ km may retain their primordial sizes. However, the only available observational statistics at the time were 25 objects of size similar to 1992 QB$_1$ and the rate of observed Jupiter-family comets (JFCs), assuming they originate from the low-inclination component of the present Kuiper Belt. Davis & Farinella (1997) argued that TNOs with diameters $D < 20$ km are significantly collisionally evolved, and produce on average 10 objects per year of size 1–10 km. Durda & Stern (2000) expanded on previous works using an updated number of discovered TNOs and estimated that 2.5 km TNOs have a collisional lifetime of 3.5 Gyr, while sub-

kilometer objects collide with 100 km TNOs once every 10^7–10^8 yr. In the intervening decades since these early works a much improved picture of the orbital structure and size distribution of the Kuiper Belt has emerged.

Surveys for Kuiper Belt objects (KBOs) (e.g., Jewitt & Luu 1993, 1995; Gladman et al. 1998, 2001; Trujillo et al. 2001; Millis et al. 2002; Jones et al. 2006; Kavelaars et al. 2009; Schwamb et al. 2010; Petit et al. 2011; Brown et al. 2015; Alexandersen et al. 2016; Bannister et al. 2016, 2018) have demonstrated that the Kuiper Belt contains a rich diversity of orbital subcomponents. Contemporary models of the formation of the Kuiper Belt imply that Neptune has played a significant role in placing and reshaping the orbits of these primordial bodies (Malhotra 1993, 1995; Levison & Morbidelli 2003; Gomes et al. 2005; Tsiganis et al. 2005; Nesvorný 2015; Shannon et al. 2019) with the orbital evolution of Neptune "fossilized" into the current state of the Kuiper Belt. Furthermore, studies of size–frequency distributions (SFDs) of the TNO subpopulations (e.g., Jewitt & Luu 1995; Gladman et al. 1998, 2001; Trujillo et al. 2001; Bernstein et al. 2004; Fraser & Kavelaars 2008; Fraser et al. 2008, 2014; Petit et al. 2011; Lawler et al. 2018b) provide clues to the agglomeration and collision history. Studied as a whole, the Kuiper Belt provides many insights into the processes of planet formation and planetary system evolution.

With the increased number of discovered TNOs more complete Kuiper Belt dynamical and physical models have become possible, allowing more precise determination of collision probabilities. Using the CFEPS L7 model (Petit et al. 2011), Dell'Oro et al. (2013) calculated the collision probabilities between different TNO populations and subpopulations, finding intrinsic collision probabilities to be lower than previous estimates. Using refined versions of the L7 model, and informed by various studies of luminosity functions, Greenstreet et al. (2015, 2016) made predictions for the collision probabilities and cratering rate onto Pluto and Charon prior to the NASA New Horizons Pluto flyby, and later Greenstreet et al. (2019) made predictions for New Horizons Kuiper Belt Extended Mission target "Arrokoth" (2014 MU$_{69}$).

There are over 1200 TNOs in the Outer Solar System Origin Survey (OSSOS) ensemble sample (Bannister et al. 2018), with high-precision orbital elements and detailed discovery characterization. This sample allows the construction of a "debiased" TNO model, using the OSSOS survey simulator (Petit et al. 2011; Lawler et al. 2018a). This improved knowledge of the structure and history of the Kuiper Belt enables further improvement of the collisional environment.

We present here our determination of the intrinsic collision probabilities between the orbital subpopulations of the Kuiper Belt based on this debiased model. The intrinsic probability is a function of the orbital distribution of objects. The orbital distribution of different dynamical TNO classes is the foundation for computing how frequently these objects collide. When combined with a TNO SFD model the intrinsic probabilities determine a collision rate. The goal of this work is to use the most up-to-date model of the Kuiper Belt orbit distribution to obtain refined collision probabilities and speeds.

In Section 2 we describe the orbital and size distributions used in our probability calculations. Section 3 presents our approach to determining the intrinsic and total collision probabilities in the current Kuiper Belt. In Section 4 we present the intrinsic collision probabilities, considering each TNO subpopulation in turn and then combining them into a total collisional probability for objects in the Kuiper Belt. In Section 5 we discuss some zeroth-order implications determined from our collisional probabilities.

2. Dynamical Structure of the Kuiper Belt

Determination of TNO orbital elements depends on accurate and multi-opposition astrometry, which is often challenging due to the large distances and faintness of TNOs (e.g., Jones et al. 2006). The apparent daily motion of a TNO, at a distance of $r \sim 40$ au, is small (mean motion $n \sim 4 \times 10^{-3}$ deg/day) and hence the observed arc ($\theta \sim 7'$), even over a month, will be a tiny fraction of the orbit. Often, observations over the course of a number of years are needed before the precise orbit of the TNO can be determined (Bannister et al. 2018). Another difficulty is introduced from the r^{-4} distance dependence of the reflected light from a TNO. Contemporary TNO detection is limited to objects with R-band magnitude brighter than $m_R \lesssim 26.5$ (Petit et al. 2006; Fraser et al. 2008) (diameter roughly $D > 30$ km), although there have been reports of detection of smaller $D \sim 1$ km TNOs using stellar occultation (Schlichting et al. 2009; Arimatsu et al. 2019). Furthermore, the rate of detection per unit area is a strong function of pointing direction: TNOs moving on highly inclined orbits have a better chance of being discovered away from the ecliptic while those on low-inclination orbits are only detectable when the observed field is near the plane of the TNO's orbit. Similarly, TNOs on eccentric orbits are more difficult to detect, brightening sufficiently only near their perihelia, but spending most of their time near aphelia. Conversely, objects on more circular orbits of moderate inclination are more readily detected. Therefore a dedicated TNO survey is more suitable and desired for extensive follow-up observations, as well as characterization of the above biases. For a review of the biases associated with TNO observations, see Kavelaars et al. (2020).

Nevertheless, since the discovery of the first TNO (Jewitt & Luu 1993), there have been a number of TNO survey programs, among them Trujillo et al. (2001), Schwamb et al. (2010), Deep Ecliptic Survey (Millis et al. 2002), Canada–France Eclipitc Plane Survey (CFEPS) (Jones et al. 2006; Kavelaars et al. 2009; Petit et al. 2011; Gladman et al. 2012), Alexandersen et al. (2016) (MA), and the OSSOS (Bannister et al. 2016, 2018; Lawler et al. 2018b). There are now $\gtrsim 3300$ cataloged TNOs in the Minor Planet Center (MPC) https://minorplanetcenter.net/iau/mpc.html, but only half of them have sufficiently well-constrained orbits to allow for precise long-term numerical integration of their orbits and accurate dynamical classification, with the majority of those coming from the OSSOS ensemble sample, which combines the CFEPS, MA, and OSSOS samples. Therefore, we choose to utilize the most up-to-date bias-free TNO dynamical model, as constrained by the OSSOS ensemble of over 1000 TNO orbits (Bannister et al. 2018).

For this work we consider the collisional circumstances for different orbit classes of TNOs. We group the TNOs into dynamical groups proposed by Gladman et al. (2008), based on long-term numerical orbital integration.

1. Resonant objects—TNOs that are currently in mean motion resonance (MMR) with Neptune.

2. Scattering objects—TNOs that experience close encounters and "scattering" off Neptune over 10 Myr of numerical orbital integration,

3. Classical and detached objects—TNOs that do not fall into either of the above categories. These are often further subdivided based on semimajor axis and inclination.

   (a) Inner belt—classical objects that are interior to the 3:2 MMR with Neptune.

   (b) Main belt—the main classical belt of TNOs, which have semimajor axes between the 3:2 and 2:1 MMRs with Neptune. The main belt contains at least two distinct subclasses: the "hot" and "cold" components, where the cold appears to be constrained to a narrow ring between 42.5 au and 44.5 au and exhibits complex substructure. The hot component is distinguished by a wide inclination (i) distribution whereas the cold component's inclinations are tightly confined, with a width of $<2°$ (Van Laerhoven et al. 2019).

   (c) Outer belt—Objects with semimajor axes beyond the 2:1 MMR and eccentricities $e < 0.24$.

   (d) Detached objects—Objects with semimajor axes beyond the 2:1 MMR and eccentricities $e > 0.24$.

To compute the collision probabilities in the Kuiper Belt we require models that describe the orbital distributions of each of these Kuiper Belt classes.

2.1. Resonant Class

As we are interested in the global collision rates we only consider those resonances with a significant number of known members and a reliable orbit distribution model available in the literature. For the sake of simplifying the computational problem, without significant loss in the precision of collisional probabilities, we compute the probabilities grouped by semimajor axis:

1. inner resonances, in order of increasing semimajor axis, N4:3, N3:2
2. main resonances (semimajor axis within the main belt resonances), N5:3 and N7:4
3. outer resonances N2:1, N7:3, and N5:2

where "N" stands for an MMR with Neptune and the convention used is p:q, where p and q are the small integers that refer to the number of orbits completed by the inner body (Neptune in our case) and the outer body (TNO) respectively; $p - q$ is referred to as the "order of resonance." Our collisional modeling does not account for the full resonant dynamics of Kozai-type orbital oscillation nor the confined precision of the argument of pericenter because we treat these objects as having uniformly precessing angular elements. However, Greenstreet et al. (2015) find that accounting for the resonant and Kozai dynamics of the plutinos leads to increases in collision probabilities and rates onto Pluto by ~50%, though as will be shown later, neglecting the nonuniform precession of the orbital elements of resonant TNOs will not change our overall conclusion.

2.2. Scattering

The orbital distribution of the scattering component can be determined via comparison with cosmogonic models of the formation of the Kuiper Belt and Oort Cloud. By definition, the orbital elements of the scattering objects are "actively" evolving. Shankman et al. (2016) and Lawler et al. (2018b) found that the currently observed orbital distributions of the scattering members of the OSSOS ensemble sample are well represented by the output of simulations in Kaib et al. (2011). We utilize the orbital distributions provided by Lawler et al. (2018b) as our orbit model for the scattering component.

2.3. Classical Kuiper Belt

Here, rather than considering parametric orbital distributions of subcomponents of the Classical Kuiper Belt we utilize an orbit model derived by debiasing a detected sample. In this way the detected Classical belt objects and the discovery survey's efficiency of detecting such orbits are used to determine the intrinsic population. For each detected orbit the likelihood of the discovery survey detecting that orbit is computed, and this likelihood is then inverted to provide the size of the intrinsic population that is implied by the particular detection. To enable this process the SFD is required and we utilize the SFD presented in Greenstreet et al. (2019). The input detected sample of classical Kuiper Belt objects and efficiencies of detection used were taken from Bannister et al. (2018). The complete orbit model will be presented in a future work.

We split the main classical belt on the basis of orbital inclination: cold-KBOs with $i < 5°$ and hot-KBOs with $i \geqslant 5°$. Here, "cold" and "hot" refer to the dynamical state of the orbits, and are not related to the objects' temperature. This arbitrary splitting is motivated by the fact that, although there is an overlap between cold and hot objects in the eccentricity and inclination space, one can see a clear concentration of objects with low inclination ($i < 5°$) (e.g., Brown 2001; Petit et al. 2011). This inclination cutoff is combined with a low eccentricity ($e < 0.08$) threshold to select out those low-i KBOs that are more strongly interacting with Neptune and group them with the hot objects for the purpose of considering average collision probabilities. We thus have two distinct TNO populations in the main classical belt, which allows us to test which of these ("hot" or "cold") is more likely to experience collisions in the Kuiper Belt.

2.4. Outer/Detached Belt

Significantly fewer nonresonant members of the Kuiper Belt have been detected with $a > 47$ au than with $a < 47$ au, making a direct debiasing statistically less certain. For this region we revert to the CFEPS L7 (Petit et al. 2011) parametric model. The L7 model represents the orbit distribution of this component as having e and i that follow the hot Main Kuiper Belt population but with a following a probability density function (PDF) $\propto a^{-5/2}$ and the remaining elements drawn randomly. The PDF of a is normalized such that the Outer/Detached component represents a smooth continuation from the hot Main Kuiper Belt. As we will see, collisions among this population are rare and the precise orbital distribution is not likely to significantly modify conclusions about impact rates.

Seven main populations are considered here—cold and hot classicals, inner resonant, main resonant, outer resonant, detached+outer belt and scattering disk—so there are 28 different orbit class combinations in total.

3. Collision Probabilities

We compute the intrinsic collision probability P_I and speeds V_I between each pair of orbits within, as well as between,

different dynamical classes. In order to compute the intrinsic collision probability between each and every TNO dynamical class, we randomly select a sample of 10^4 orbits from orbital distributions in each subpopulation. The intrinsic collision probability is independent of the sample size, but larger samples provide somewhat better sampling of the available phase space for the orbit class being considered. For each orbit family pair we computed the intrinsic collision probability between each pair of orbits in each population: the number of calculations roughly scales as $\sim N^2$, where N is the number of individual orbits considered. Each probability computation required an average CPU time of $t \sim 1.5$ ms per orbit pair. Performing tests with different sample sizes, we concluded that computation between 10^4 orbits, which is equivalent to $\sim 5 \times 10^7$ orbit pairs (requiring about 20 hr of computing) provided statistically equivalent behavior to a sample of 10^5 (requiring about 200 hr of computing). We then compute the intrinsic collision probabilities between each of the 28 permutations of our orbit classes.

We use the approach described in Wetherill (1967) to compute the intrinsic collision probability between two orbits:

$$P_I = \frac{V_I R_h}{8\pi^2 \sin i' |\cot \alpha| a_1 a_2 \sqrt{p_1 p_2}},$$
$$p_1 = a_1(1 - e_1^2)$$
$$p_2 = a_2(1 - e_2^2)$$
$$R_h = \frac{p_2}{1 + e_2 \cos \omega}$$
$$\cot \alpha = R_h \dot{\omega}/\dot{R_h} \qquad (1)$$

where p_1 and p_2 are the semi-latus rectums of the two orbits, i' is the mutual inclination, and V_I is the relative velocity between the two bodies at the point of orbit intersection. The distance R_h is the heliocentric distance of the intersection point (mutual node) of the two orbits and ω is the orientation of perihelion of the impacting orbit and has the meaning of true anomaly of the intersection point. α is the angle between object's rectilinear trajectory and the heliocentric distance vector. The intrinsic collision probability is a function of the orbital elements of the given orbit pair only, without involving their size. Due to gravitational perturbations, the arguments of pericenter and the longitudes of the ascending node of the two orbits will experience secular variations, causing the mutual inclination between the two orbits to process. Equation (1) does not incorporate the longitude of the ascending node and the argument of pericenter, because the formalism of Opik (1951) and Wetherill (1967) assumes that all values for these parameters, during one procession cycle, are equally probable.[11]

For the computations we make use of the FORTRAN implementation used by Greenstreet et al. (2015) to calculate the collision probabilities and speeds between each orbit pair within and between different TNO populations. However, we extended this code to provide the intrinsic collision probability as both a function of speed (as in Greenstreet et al. 2015) and a function of the heliocentric distance at the time of collision. We provide our results as a matrix of 200×135 (200 distance

bins $\times$ 135 velocity bins), where each cell has dimension 1 au $\times$ 0.1 m s^{-1}. The full grid of collision probabilities is provided in electronic form.

The results of the calculated intrinsic collision probability P_I and speeds V_I, between and within different TNO populations, are summarized in Figures 1–3. Each pixel in each subplot is color-coded in terms of the intrinsic probability P_I [in km^{-2} yr^{-1} TNO^{-1}] of a collision occurring with a speed V_I [in km s^{-1}] at a given heliocentric distance R_h [in au]. Given the large range of variation of ΔP_I (over seven orders of magnitude), the data in each plot are presented on a logarithmic scale. In addition, we also provide separately the probability density of a collision happening with a given impact speed V_I, for the different dynamical TNO populations (Figure 6). The intrinsic collision probabilities between each TNO population, i.e., the average of all pixel values for each subplot, are summarized in Table 1. The intrinsic probabilities must be multiplied by the size of the populations to determine the collision rate. The probability plots provide a quick visualization of where in the Kuiper Belt collisions are most likely to occur and which orbital classes have the largest intrinsic probability of collisions.

Our calculated intrinsic probabilities and speeds indicate that collisions in the Kuiper Belt are possible over a wide range of heliocentric distances $R_h = 30–200$ au and speeds $V_I < 9$ km s^{-1}, though the majority of these collisions are expected to occur in a narrow range between $R_h = 30–55$ au and with much lower speeds (see Figures 1, 2, and 3). Although we see collision speeds as high as 9 km s^{-1}, they are very unlikely to occur over the age of the solar system, with speed $V_I < 6$ km s^{-1} being more likely (Figure 6).

The highest intrinsic collision probability occurs within the "cold" subcomponent of the classical belt, followed by the "hot" on "cold" impacts, and within the "hot" substructure. This is not surprising given that these populations are more concentrated in the orbit phase space than the other orbit classes considered. It is also evident that the cold classicals collide with median velocity $\langle V_I \rangle \approx 0.3$ km s^{-1} and have a narrow range of impact speed (see Figure 6(a)). That raises an interesting question as to whether the collisions between these objects are disruptive, crater-forming, or result in complex structure formation. The expectation of low impact velocities is similar to the result reported in Greenstreet et al. (2019) when considering impacts onto Arrokoth and utilizing the CFEPS L7 orbit model.

We also note a bimodality in the impact speed distribution for "hot" on "cold" collisions (Figure 6(a)). The reason for this is the existence of substructures in the semimajor axis distribution of the "cold" and "hot" subcomponents of the main belt creating distinct subsets of collisional circumstances. A bimodal velocity distribution is also seen for the scattering population colliding with the "cold" substructure of the main belt (Figure 6(d)). This structure also appears to be due to the substructure in the semimajor axis distribution of the "cold" population.

The intrinsic probabilities we report here are consistent (within an order of magnitude) with those reported in Dell'Oro et al. (2013), who performed similar analysis using the CFEPS L7 model. The impact speeds reported in Dell'Oro et al. (2013), however, are somewhat ($\sim$70%) higher than the values reported here and in Greenstreet et al. (2019) (which were also derived using the CFEPS L7 model).

---

[11] We do not consider the effects of resonant dynamics of the colliding objects because these do not strongly alter interclass collisional probabilities.
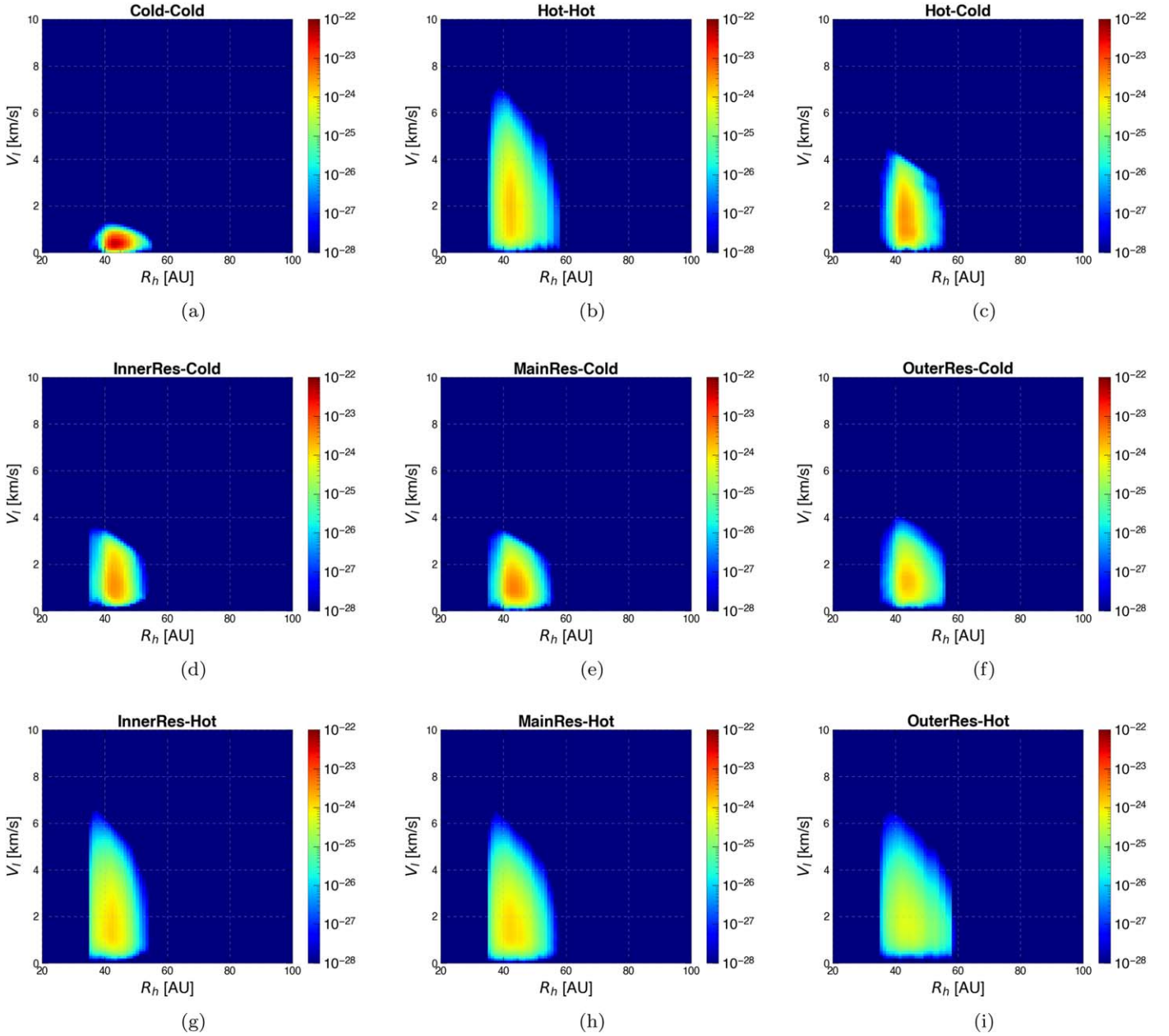
Figure 1. Intrinsic collision probabilities P_I (color bar) with a given collision speed V_I at a given heliocentric distance R_h between different dynamical TNO classes. The intrinsic collision probability in each cell is color-coded and has units $km^{-2} yr^{-1} TNO^{-1}$. The values of the color bars only include values $P_I > 10^{-28} km^{-2} yr^{-1}$, because smaller values are unlikely to result in collision over the age of the solar system (see text for details).

3.1. Combined Intrinsic Probabilities

P_I for the Kuiper Belt can now be determined by combining together the P_I for the various subcomponents determined in the previous section. To do this we must first weight each probability matrix by the relative size of the the components of the Kuiper Belt population involved. Frustratingly, the actual relative sizes of these populations depend on the size range of subpopulations being considered. The "Excited" members of the Kuiper Belt (the Hot Classical Kuiper Belt, Resonant objects, Scattering disk, and Outer/Detached components) appear to have one size distribution while the SFD of the cold Classical Kuiper Belt appears to be different. In Table 2 we summarize population estimates in the current literature of the various orbit classes in the Kuiper Belt, down to the sizes of objects for which reasonably secure estimates of the populations are available. We use the fractional population estimates of the subclasses to combine together the P_I grids for the individual components and determine a global map of P_I for the Kuiper Belt region (Figure 4).

4. Collision Rates

The "final" collision probability ($yr^{-1} TNO^{-1}$) between two objects of radii r and R is obtained by multiplying Equation (1) by the cross-sectional area of the two objects, e.g., $P_F = P_I \times A = P_I(r + R)^2$. We remind the reader that the factor of π in the cross-sectional area is incorporated in P_I.

To obtain the number of collisions N_c, per unit time, for an ensemble of objects in a given size range, P_F needs to be integrated over a suitable size distribution, representing the number of objects relevant for these populations. For example,
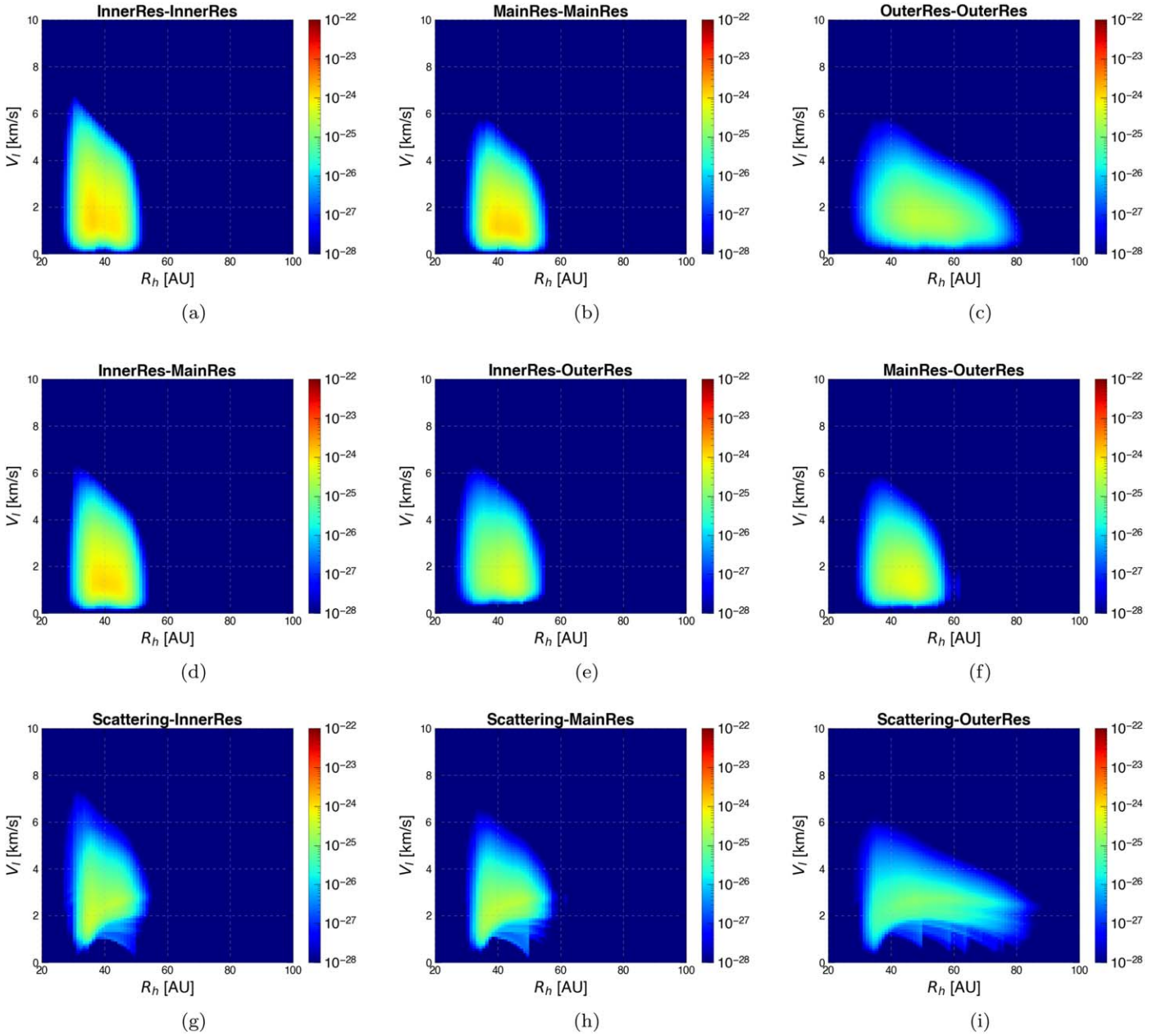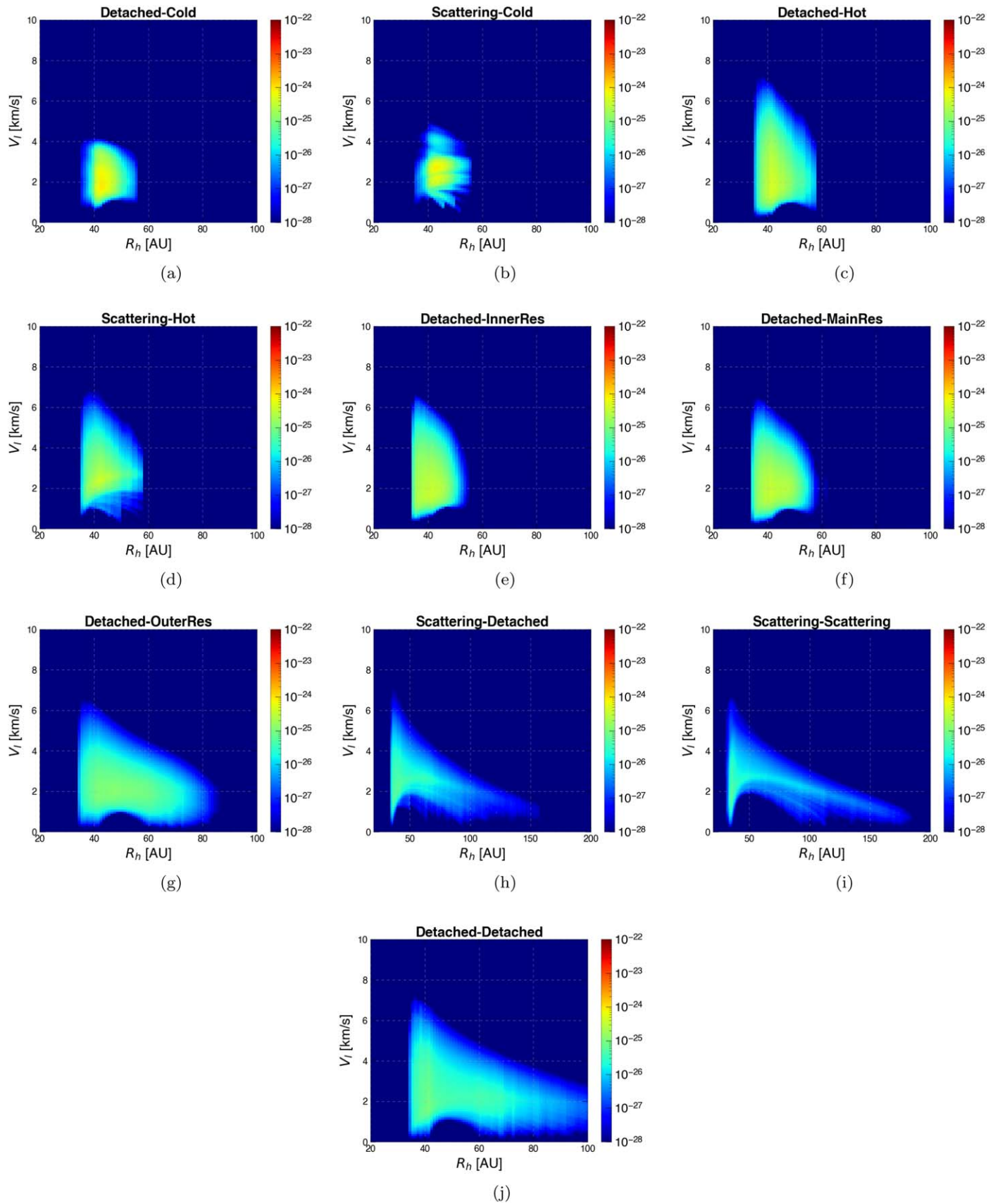
Figure 2. Intrinsic collision probabilities P_I (color bar) with a given collision speed V_I at a given heliocentric distance R_h between different dynamical TNO classes. The intrinsic collision probability in each cell is color-coded and has units $km^{-2} yr^{-1} TNO^{-1}$. The values of the color bars only include values $P_I > 10^{-28} km^{-2} yr^{-1}$, because smaller values are unlikely to result in collision over the age of the solar system (see text for details).

the number of collisions N_c, per unit time, that a single target of size $R = 50$ km would experience, with a given TNO population in a given size range $r_1 < r < r_2$, scales as the intrinsic collision probability between the target and objects from the given orbit class as well as the size and number of impactors per unit size in that class. In a given impactor size range, the number of collisions with a single 50 km target will be

$$N_c = P_I \int_{r_1}^{r_2} (50 + r)^2 \frac{dN}{dr} dr \qquad (2)$$

where dN/dr is the number of impactors with size between r and $r + dr$ for the given TNO orbit class. If one is interested in

the total number of collisions between all members of two orbit classes then one must integrate over both size distributions:

$$N_c = P_I \int_r \int_R (r + R)^2 \frac{dN}{dr} \frac{dN}{dR} dr dR \qquad (3)$$

where dN/dr and dN/dR are the impactor and target size distributions.

If one is interested in the number of collisions over a given time interval, Equation (3) is then multiplied by that time interval.

The SFD for Kuiper Belt populations can be approximated using exponential distributions of the form $dN/dr \propto r^{-q}$. The

Figure 3. Intrinsic collision probabilities P_I (color bar) with a given collision speed V_I at a given heliocentric distance R_h between different dynamical TNO classes. The intrinsic collision probability in each cell is color-coded and has units $km^{-2} \, yr^{-1} \, TNO^{-1}$. The values of the color bars only include values $P_I > 10^{-28} \, km^{-2} \, yr^{-1}$, because smaller values are unlikely to result in collision over the age of the solar system (see text for details).

Table 1
Intrinsic Collision Probability $\langle P_I \rangle$ and Speeds V_I by Subcomponent

Population	$\langle P_I \rangle$ (km^{-2}	Relative $\langle P_I \rangle$[a]	V_I (km s^{-1})[b]		
Target–Impactor	yr^{-1})	(%)	0.05	0.50	0.95
Cold Classical					
Cold–Cold	7.5e-22	16.6	0.1	0.3	0.7
Cold–Hot	3.2e-22	7.1	0.6	1.4	3.0
Cold–Inner res	2.6e-22	5.8	0.5	1.3	2.7
Cold–Main res	3.0e-22	6.7	0.4	1.0	2.1
Cold–Outer res	1.6e-22	3.6	0.5	1.2	2.5
Cold–Detached	7.7e-23	1.7	1.3	2.1	3.4
Cold–Scattering	4.7e-23	1.0	1.8	2.6	3.5
Hot Classical					
Hot–Hot	2.9e-22	6.4	0.6	2.0	4.4
Hot–Inner res.	2.3e-22	5.1	0.5	2.5	3.7
Hot–Main res.	2.5e-22	5.5	0.6	1.8	3.8
Hot–Outer res.	1.1e-22	2.4	0.7	1.8	3.8
Hot–Detached	8.3e-23	1.8	1.1	2.4	4.7
Hot–Scattering	4.4e-23	1.0	1.8	2.7	4.5
Resonant					
Inner res.–Inner res.	3.2e-22	7.1	0.8	2.0	4 .3
Inner res.–Main res.	2.6e-22	5.8	0.7	1.7	3.7
Inner res.–Outer res.	1.0e-22	2.2	0.9	1.9	3.9
Main res.–Main res.	2.6e-22	5.8	0.6	1.5	3.1
Main res.–Outer res.	1.2e-22	2.7	0.8	1.7	3.2
Outer res.–Outer res.	9.2e-23	2.0	0.7	1.6	3.1
Scattering					
Scattering–Inner res.	6.1e-23	1.4	1.6	2.8	4.7
Scattering–Main res.	5.5e-23	1.2	1.6	2.7	4.1
Scattering– Outer res.	3.3e-23	0.7	1.7	2.8	4.1
Scattering–Detached	2.3e-23	0.5	1.5	2.6	4.0
Scattering– Scattering	1.6e-23	0.4	1.7	2.8	4.5
Detached/Outer					
Detached–Inner res.	7.8e-23	1.7	1.2	2.2	3.9
Detached–Main res.	8.2e-23	1.8	1.2	2.2	4.0
Detached–Outer res.	5.2e-23	1.2	1.1	2.2	4.0
Detached–Detached	3.8e-23	0.8	1.1	2.2	4.4

Notes.
[a] Fraction of total intrinsic probability, not including relative population sizes.
[b] The distribution of the collision speeds between different TNO populations: the 5th (left column), the 50th (middle column), and 95th (right column) percentiles, respectively.

size distribution does not follow a single power law from the smallest to the largest bodies, but can be described using a small number of different logarithmic slopes, each valid for a given size range (e.g., Bernstein et al. 2004; Petit et al. 2008, 2011; Fraser et al. 2014). For a given impactor TNO population, the number of collisions N_{ct} that a target of $R = 50$ km would experience in a given time T will be the sum over the different logarithmic slopes appropriate to those impactors multiplied by the P_I appropriate to the target and impactor orbital classes being considered. That is,

$$N_{ct} = T P_I \sum_i \left[\int_{r_{1i}}^{r_{2i}} (50 + r)^2 \left(\frac{r}{r_{oi}} \right)^{-q_i} dr \right] \qquad (4)$$

where r_{1i} and r_{2i} are the limits of the range over which the logarithmic slope q_i is valid and r_{oi} is the normalization. The total number of collisions can be obtained by adding the

Table 2
Estimates of TNO Subcomponent Populations

Orbit Class	Fraction (% of Total)	Population $N(H_r < 8.66)$
Cold Main Belt	20	$61{,}000 \pm 6000$
Hot Main Belt	12	$38{,}000 \pm 9000$
Detached/Outer	26	$80{,}000 \pm 40{,}000$
Scattering	29	$90{,}000 \pm 20{,}000$
Inner resonances		
4:3	0.1	400^{+800}_{-120}
3:2	4.2	$13{,}000^{+6000}_{-5000}$
Main resonances		
5:3	1.6	5000^{+5200}_{-3000}
7:4	0.9	3000^{+4000}_{-2000}
Outer resonances		
2:1	1.2	3700^{+4400}_{-2400}
7:3	1.3	4000^{+8000}_{-3000}
5:2	3.8	$12{,}000^{+15000}_{-8000}$

References: Petit et al. (2011), Lawler et al. (2018b), Gladman et al. (2012).

contributions from each TNO population:

$$N_t = \sum_j N_{cj}$$
$$= T \sum_j P_{Ij} \sum_i \left[\int_{r_{1ij}}^{r_{2ij}} (50 + r)^2 \left(\frac{r}{r_{oij}} \right)^{-q_{ij}} dr \right] \qquad (5)$$

where N_{cj} denotes the contribution of a given TNO population to the number of collisions. Similarly, P_{Ij} is the intrinsic collision probability between a given target and TNO population.

To provide a sense of the frequency of collisions in the Kuiper Belt and to compare our calculated collision probabilities to previous works (e.g., Greenstreet et al. 2015, 2016) we present an estimate of the total number of *impacts* on an $R = 50$ km target. A precise estimate of the total number of collisions that a particular target of $R = 50$ km would experience depends naturally on the orbital elements of the target and the impactor population it could collide with as well as the gravitational focusing and acceleration due to non-negligible mass of the target body. By considering a small target ($R = 50$ km) we are able to neglect gravitational focusing. For our orbit we use mean collision probabilities for two target populations. We compute the total number of impacts that a mean "inner resonant object" (IRO, our combined 4:3 and 3:2 resonant populations) and a mean "cold Classical Kuiper Belt Object" (CCKBO) would experience in the current Kuiper Belt. The mean impact rates determined here should be roughly similar when compared to more direct computations for specific bodies.

In addition, considering a specific size range of impactors allows for approximate comparison with crater counts on the Pluto–Charon system (Singer et al. 2019) and Arrokoth (Spencer et al. 2020). For Charon, impactor size scales with crater size as $d = 0.07 D^{1.151}$ where d and D are the impactor and crater sizes in kilometers (Singer et al. 2019, Table S2). Using this relation we determine that the craters with $1.4 \, \text{km} < D < 10 \, \text{km}$ measured on the smooth area of Charon's Vulcan Planum (Singer et al. 2019, Table S2) correspond roughly to impactors of $100 \, \text{m} \lesssim d \lesssim 1 \, \text{km}$. For Arrokoth the New Horizons team reported craters in the size range
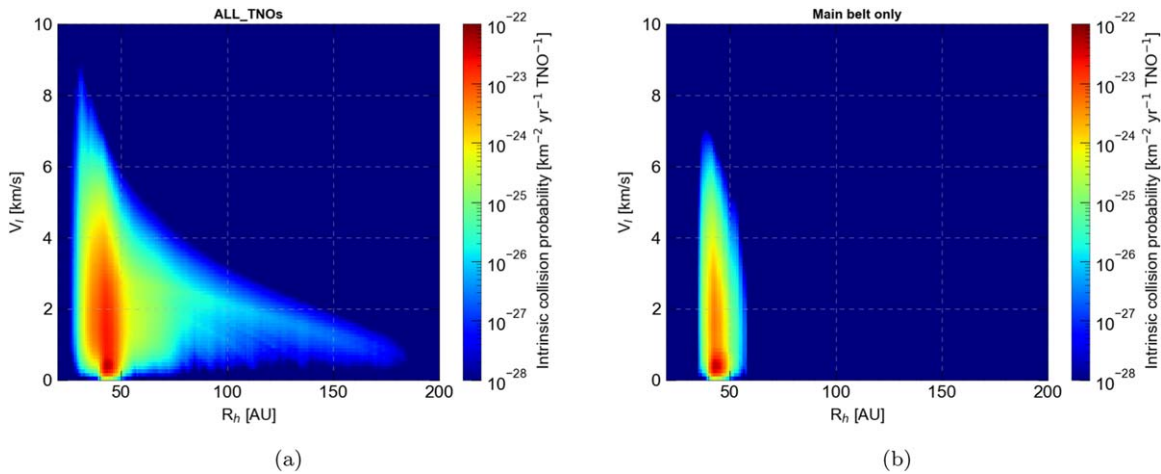
Figure 4. Combined collision probability (color bar) as a function of the heliocentric distance R_h and impact speeds V_I between all TNO populations (a) and the main Kuiper Belt only (b). Subplot (a) is essentially the sum of all subplots in Figures 1, 2, and 3, while subplot (b) presents the intrinsic collision probabilities between "cold–cold," "hot–hot," and "hot–cold" subclasses. Each 2D pixel in each subplot has dimensions of 100 m s^{-1} × 1 au.

$200\,\mathrm{m} < D < 1\,\mathrm{km}$, which translates to impactor sizes $2\,\mathrm{m} < r < 10\,\mathrm{m}$. This choice of size range roughly maps to impact crater sizes $1.4\,\mathrm{km} < D < 10\,\mathrm{km}$ (Singer et al. 2019) observed on Charon and to sizes $0.2\,\mathrm{km} < D < 1\,\mathrm{km}$ (Spencer et al. 2020) on Arrokoth, using impact cratering scaling laws from Zahnle et al. (2003), a relationship also adopted by Greenstreet et al. (2015, 2016). To determine the total number of impactors in these size ranges requires knowing the SFD of objects in each impactor group. Petit et al. (2011) provides population estimates for magnitude $H_g < 8$, which we convert to H_r using the color index $(g - r) = 1.0$ for the cold and $(g - r) = 0.8$ for the hot TNO components (e.g., Schwamb et al. 2019). The impactor sizes considered here are within the absolute magnitude range $17 < H_r < 32$ in the r band with the exact conversion dependent on choice of albedo, discussed below. The number of objects in the range $8.66 < H_r < 17$ for both high- and low-inclination TNOs was then estimated using a single logarithmic slope of $\alpha = 0.4$ (or $q = 5\alpha + 1 = 3$), extrapolating smoothly from $N(H_r < 8.66)$ in Table 2, i.e., we did not consider a size-frequency distribution with a divot (Shankman et al. 2016) as was explored in Greenstreet et al. (2016, 2019).

For the range $17 < H_r < 32$ we use an average slope of $\alpha = 0.2$ ($q = 2$) based on the slope in the crater size–frequency distribution seen on Charon ($q = 1.8 \pm 0.2$) (Singer et al. 2019) and Arrokoth ($q = 2.3 \pm 0.6$) (Spencer et al. 2020). To convert absolute magnitude to impactor and target size, albedos of 0.14 and 0.08 were assumed for the low- and high-inclination populations.

Using population sizes and collision probabilities for our subpopulation groups we then compute the total impact rate onto our nominal IRO and CCKBO objects. Our model predictions of the number of collisions, distributed by velocity and heliocentric distance, that a single target of size $R = 50\,\mathrm{km}$ belonging to the inner resonant and CCKBO populations would experience over the age of the solar system are presented in Figures 5(a) and (b). These impact distributions differ somewhat from each other and provide an indication of where within the Kuiper Belt each subpopulation is experiencing collisions, and thus where those populations are most likely to be the source of local dust. In particular we note that for the IRO orbit a significant number of impacts occur interior to

40 au, and those impacts in the 40 au to 45 au zone have speeds of between 0.7 km s^{-1} and 3 km s^{-1}, while for the CCKBO almost no impacts occur interior to 40 au and the bulk of impacts are in the 40–50 au zone with impact speeds well below 1 km s^{-1}.

For the case of an IRO, a 50 km spherical body (surface area $\sim$31,000 km^2), our model predicts $N_{\mathrm{tot}} \sim 12$ impacts over the age of the solar system, with impactors in the range 0.01 km $< r < 1$ km (Figure 5(a)). The New Horizons science team reported 70 craters with size $1.4\ \mathrm{km} < D < 10\,\mathrm{km}$ on the smooth terrain of Charon's Vulcan Planitia (see supplementary material in Singer et al. 2019). Vulcan Planitia subtends an area of roughly $A \sim 35{,}000\,\mathrm{km}^2$ (Singer et al. 2019) or $\sim$10% larger than the surface area of a 50 km target body, increasing our calculated total number of impacts by 10% from to 12 to 13. We find that the impact rate onto a typical IRO is dominated ($\sim$35%) by the cold classical TNO population, followed by the hot ($\sim$21%) and detached ($\sim$17%) subgroups. A similar trend was observed in the analysis of Greenstreet et al. (2015, 2016). We find that the inner resonance population accounts for only $\sim$14% of the total impact rate on our nominal IRO. The offset between our predicted number of impacts and the observed number of craters on Charon, aside from uncertainties in the population estimate and SFD, is further affected by ignoring the following points.

1. We note that our model is designed to calculate the collision probability within and between different groups of TNO populations, as opposed to using the exact orbit of Charon.

2. Our comparison of the number of impacts onto a 50 km target with the number of craters does not reflect the actual impact rate onto Charon. We neglect the gravitational focusing term $(1 + V_{\mathrm{esc}}^2/V^2)$ in our example due to the smaller size of our target, though the gravitational focusing effect is important for Charon-sized bodies. In fact, we find that the gravitational focusing effect for Charon will increase the impact rate by $\sim$20%. That implies, if we used a Charon-sized target body in our calculations, that the actual number of impacts onto an area of 35,000 km^2 must be about 20% greater than 13, i.e., $\approx$16.
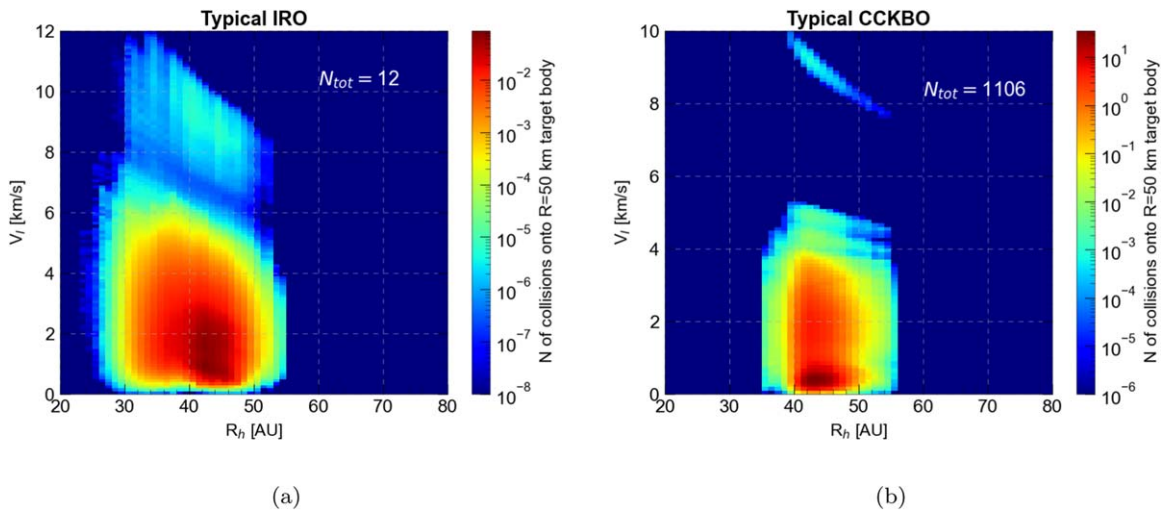
Figure 5. Number of collisions (color bar) with an average "plutino" (a) and with a typical "cold Classical Kuiper Belt Object" (b). In both cases the target is assumed to have radius $R = 50$ km. The total number N_{tot} of impacts is estimated over 4 Gyr, with impactors in the ranges 100 m $< r < 1$ km (a) and 2 m $< r < 10$ m (b). Each 2D pixel in each subplot has dimensions of 100 m s^{-1} $\times 1$ au. The discontinuity and small contribution to high-speed impacts ($V_I > 8$ km s^{-1} in both plots) are attributed to the "granularity" in our scattering population model.

3. In this work we ignore the full resonant and "Kozai–Lidov" dynamics of Charon's orbit, although we do add a correction factor of 1.5 (Greenstreet et al. 2015, 2016) to the collision rates of plutinos onto Charon. Both of these effects will add to nonuniform precession of the orbital elements, as well limit the range that the orbital elements can span over a precession cycle, effectively resulting in an increased rate of encounters with other TNOs.

4. We have failed to precisely model the relationship between impactor flux and number of observed craters. Impact scaling laws suggest that, aside from the size of the colliding objects, there is a strong correlation between the impact speed, gravitational acceleration of the target, and bulk densities of the target and impactor (e.g., Holsapple et al. 2002; Housen & Holsapple 2003, 2011; Zahnle et al. 2003; Housen et al. 2018). We convert observed impact crater diameters on Charon to impactor size using an average collision speed of 2 km s^{-1} for all populations. However, Figure 6 shows that the distributions of collision speeds between some TNO populations exhibit long tails with V_I in excess of 3 km s^{-1}. The effect of using an average impact speed, as opposed to a detailed distribution, in the conversion from crater to impactor size will underestimate the size range of impactors considered in this work, which will translate to reduced total impactor flux.

For a detailed analysis of the impact rates onto a single object, the above shortcomings must be accounted for, as in Greenstreet et al. (2015, 2016). Recognizing the uncertainties associated with TNO population estimates and in the SFD of objects smaller than 10 km, as well as neglecting the above-mentioned points, our results give confidence in the collision probabilities calculated between different TNO classes. In a subsequent work, we will explore the actual collision rates in the trans-Neptunian region, which urges consideration of the above shortcomings that are associated with our sample calculations of collision rates.

For the case of a CCKBO, a target of radius $R \sim 50$ km (surface area $\sim$31,000 km^2) is expected to be impacted $\sim$1100 times, with impactors in the size range 2 m $< r < 10$ m, over

the age of the solar system. The New Horizons team has counted 43 craters, over a surface area of 700 km^2, on the encounter hemisphere of Arrokoth, with sizes in the range 0.2 km $< D < 1$ km (Spencer et al. 2020). But the surface area used for counting craters on Arrokoth (700 km^2) is only 2.3% of that of a spherical 50 km target body, so our modeling predicts $N_{tot} = 1100 \times 0.023 \approx 25$ craters on that area of Arrokoth. Unlike the IRO case, we find a better agreement with observations. The reason is that the low-inclination component of the main classical Kuiper Belt is more tightly confined near the ecliptic, effectively resulting in a higher collision probability within the cold population and with other TNO groups. Furthermore, Arrokoth is expected to be primarily impacted by the cold classical TNOs, which display a tighter impact speed probability distribution, where the assumed average impact speed $V_i = 0.3$ km s^{-1} is a good assumption for the overall spread of impact speeds. This is further supported by our finding that 56% of the impacts onto our nominal CCKBO are attributed to the cold classicals. We also find that the hot population is the next most dominant impactor flux on our typical CCKBO, contributing $\sim$17% of the total impact rate, followed by the detached ($\sim$10%) and inner resonant ($\sim$8%) populations. The population contributing the least to the total impact flux is the scattering population, accounting for $\sim$2%.

Finally, based on our modeling and analysis we find that most TNO collisions occur in the main classical belt, with the intrinsic collision probability for this subcomponent accounting for $\sim$30% (see Table 1) of the average total collision probability $\langle P_I \rangle \approx 4.5 \times 10^{-21}$ km^{-2} yr^{-1} TNO^{-1} within the TNO population. Within the main classical belt, collisions are dominated by "cold" on "cold" impacts ($\sim$17%) with median impact speeds $\langle V_I \rangle \sim 0.3$ km s^{-1}. The next most important source of impacts are the resonant TNOs (taking all resonances together), which account for $\sim$26% of the total collision probability. Resonant TNOs experience collisions at speeds in excess of 1 km s^{-1} and may be more significant sources of dust than the impacts within the "cold" population. In contrast, we find that the collision probabilities within the scattering population are almost four orders of magnitude lower than
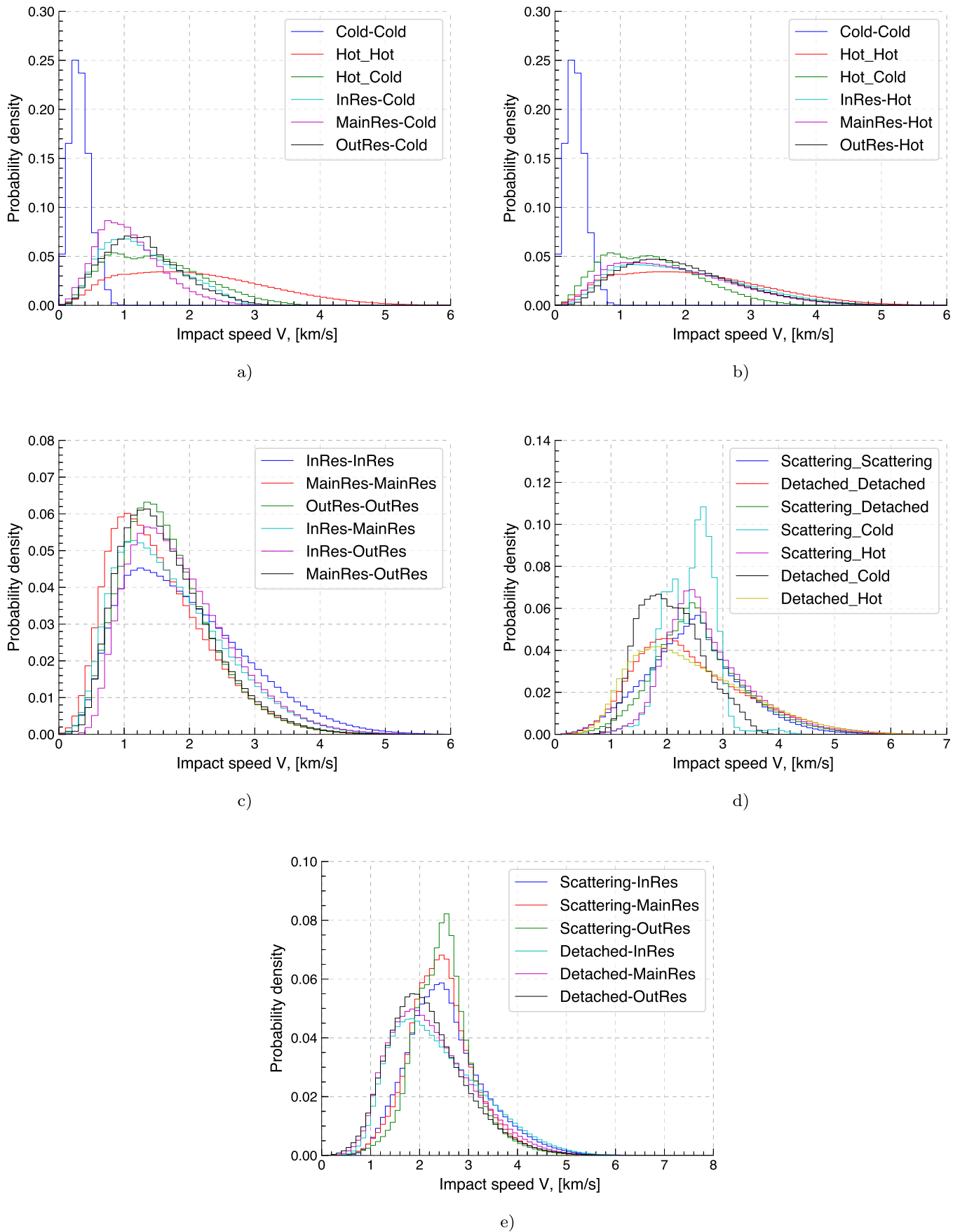
Figure 6. Probability density of the impact speeds between different dynamical TNO populations. All plots have been normalized to unity.

those in the main classical belt (Table 1; see also Figures 1(a) and 3(i)). These results provide a strong proxy for where in the Kuiper Belt the dust production is expected to dominate. Models of dust production and general cratering among TNOs will need to take into account the differences in collisional probabilities between the two major sources of impacts.

5. Discussion and Conclusions

We have calculated the intrinsic collision probabilities and the corresponding impact speeds between different TNO populations, based on a revised dynamical model of the Kuiper Belt, derived from the OSSOS ensemble sample, finding that low-velocity impacts at distances $30 < R_h < 50$ au are most likely.

Our calculations indicate that collisions are concentrated in the main Kuiper Belt region (30–55 au) but impacts over a wide range of distances (30–150 au) are not excluded. Although our simulations indicate collision speeds in excess of 8 km s^{-1}, most of the collisions are likely to happen with speeds well below $V_I < 5$ km s^{-1}, over the age of the solar system.

The highest intrinsic collision probability, $P_I \sim 7.5 \times 10^{-22}$ km^{-2} yr^{-1} TNO^{-1}, is observed for impacts within the cold main classical population, with these collisions occurring at the lowest median speed $\langle V_I \rangle \sim 0.3$ km s^{-1}, and accounting for ~17% of the average total collision probability $\langle P_I \rangle \approx 4.5 \times 10^{-21}$ km^{-2} yr^{-1} TNO^{-1} of all TNO populations. The dominance of impacts in the cold classical belt is not particularly surprising because these objects spend more time physically proximate to each other and close to the ecliptic, compared to the hot classical, scattering, and resonant objects, whose orbits carry them over large ranges of heliocentric distance, resulting in lower overall space density within these orbital classes. The low impact velocities among objects with the highest impact probabilities result from the narrower distributions of semimajor axis, eccentricity, and inclination of main classical KBOs, compared to the detached and scattering populations. Moreover, the highest impact speeds between the cold objects do not exceed 1 km s^{-1}, raising a fair question as to whether these collisions are catastrophic or even crater-forming. The outcome of a collision is a strong proxy for the amount of material (dust) liberated in these impact events. Perhaps, due to the low impact speeds, collisions within the cold classical population are most likely to lead to crater formation rather than to a complete disruption of colliding bodies. Furthermore, the low impact speeds may also favor slow merging of cold KBOs into a single binary object.

The next highest collision probability ($P_I = 3.2 \times 10^{-22}$ km^{-2} yr^{-1} TNO^{-1}) is observed between the hot and cold populations, with a contribution of ~7% of the total average intrinsic collision probability, though with noticeably higher impact speeds. In a subsequent work, we will investigate whether these higher impact speeds are destructive, accounting for the specific impact energy involved. Although somewhat lower in probability, collisions between hot and cold classical KBOs may very well dominate the dust production in the Kuiper Belt, given their impact speeds.

We see a bimodality in the velocity distribution for collisions between the scattering and cold populations, which could be a sampling "artifact" caused by the low fidelity of our input scattering model. A few outliers with high inclination and eccentricity of the scattering model distribution are over-contributing to the probability distribution. The gap in probabilities is not evident for all orbital populations and tends

to be more prominent for impactors with high eccentricity and semimajor axis dispersion, which the relative velocity is a strong function of. A few such orbits whose semimajor axes overlap due to numerical resolution can lead to granularity in the computed impact velocity distribution.

The lowest collision probability appears to happen within the scattering and detached populations with median collision speeds in excess of 2 km s^{-1}. Collision at these speeds may result in impactor and target fragmentation, as opposed to cratering and simple ejecta, depending on the size of the colliding bodies. Given the low intrinsic probability and total number of objects on these orbits, the likelihood of collisions, even after 4 Gyr of evolution in the TNO population, is now very low. Collisions among these populations may have produced significant levels of dust early in the solar system's history when the number objects on such orbits would have been tens to hundreds of times higher.

Similar to Dell'Oro et al. (2013), we find that P_I is indeed lower than previously reported values (e.g., Davis & Farinella 1997), though our computed collision speeds differ slightly from Dell'Oro et al. (2013). We find that the cold main classicals collide on average with speeds $\langle V_I \rangle \sim 0.3$ km s^{-1}, about 40% lower than those obtained by Dell'Oro et al. (2013). Similarly, our impact speed between the hot components of the main belt ranges from 0.6 to 4.4 km s^{-1}, with a median value of $\langle V_I \rangle \sim 2.0$ km s^{-1}, whereas the value reported by Dell'Oro et al. (2013) is ~20% higher. The most likely reason for that is that we report the median collision speed, based on Öpik and Wetherill's formalism of collisions between asteroids, whereas the aforementioned authors provide results from the best fit to Monte Carlo simulations.

We have also provided approximate expected numbers of impacts onto a 50 km sample plutino and CCKBO and compared them to the observed crater densities on Charon and Arrokoth found by the New Horizons spacecraft. We find that our results display a good agreement with crater densities reported by New Horizons, and are also in agreement with the results first predicted by Greenstreet et al. (2015, 2016, 2019).

ORCID iDs

Abedin Y. Abedin ⓘ https://orcid.org/0000-0002-7025-0975
J. J. Kavelaars ⓘ https://orcid.org/0000-0001-7032-5255
Sarah Greenstreet ⓘ https://orcid.org/0000-0002-4439-1539
Jean-Marc Petit ⓘ https://orcid.org/0000-0003-0407-2266
Brett Gladman ⓘ https://orcid.org/0000-0002-0283-2260
Samantha Lawler ⓘ https://orcid.org/0000-0001-5368-386X
Mike Alexandersen ⓘ https://orcid.org/0000-0003-4143-8589
Ying-Tung Chen ⓘ https://orcid.org/0000-0001-7244-6069
Kathryn Volk ⓘ https://orcid.org/0000-0001-8736-236X

References

Alexandersen, M., Gladman, B., Kavelaars, J. J., et al. 2016, AJ, 152, 111
Arimatsu, K., Tsumura, K., Usui, F., et al. 2019, NatAs, 3, 301
Bannister, M. T., Gladman, B. J., Kavelaars, J. J., et al. 2018, ApJS, 236, 18
Bannister, M. T., Kavelaars, J. J., Petit, J.-M., et al. 2016, AJ, 152, 70
Benz, W., & Asphaug, E. 1999, Icar, 142, 5
Bernstein, G. M., Trilling, D. E., Allen, R. L., et al. 2004, AJ, 128, 1364
Brown, M. E. 2001, AJ, 121, 2804
Brown, M. E., Bannister, M. T., Schmidt, B. P., et al. 2015, AJ, 149, 69
Charnoz, S., Canup, R. M., Crida, A., & Dones, L. 2018, in Planetary Ring Systems: Properties, Structure, and Evolution, ed. M. S. Tiscareno & C. D. Murray (Cambridge: Cambridge Univ. Press), 517
Charnoz, S., Morbidelli, A., Dones, L., & Salmon, J. 2009, Icar, 199, 413
Davis, D. R., & Farinella, P. 1997, Icar, 125, 50
Dell'Oro, A., Campo Bagatin, A., Benavidez, P. G., & Alemañ, R. A. 2013, A&A, 558, A95
Durda, D. D., & Stern, S. A. 2000, Icar, 145, 220
Fraser, W. C., Brown, M. E., Morbidelli, A., Parker, A., & Batygin, K. 2014, ApJ, 782, 100
Fraser, W. C., & Kavelaars, J. J. 2008, Icar, 198, 452
Fraser, W. C., Kavelaars, J. J., Holman, M. J., et al. 2008, Icar, 195, 827
Fujiwara, A., Cerroni, P., Davis, D. R., et al. 1989, in Asteroids II, ed. R. P. Binzel, T. Gehrels, & M. S. Matthews (Tucson, AZ: Univ. Arizona Press), 240
Gladman, B., Kavelaars, J. J., Nicholson, P. D., Loredo, T. J., & Burns, J. A. 1998, AJ, 116, 2042
Gladman, B., Kavelaars, J. J., Petit, J.-M., et al. 2001, AJ, 122, 1051
Gladman, B., Lawler, S. M., Petit, J. M., et al. 2012, AJ, 144, 23

Gladman, B., Marsden, B. G., & Vanlaerhoven, C. 2008, in The Solar System Beyond Neptune, ed. M. A. Barucci, H. Boehnhardt, D. P. Cruikshank, & A. Morbidelli (Tucson, AZ: Univ. of Arizona Press), 43
Gomes, R., Levison, H. F., Tsiganis, K., & Morbidelli, A. 2005, Natur, 435, 466
Greenstreet, S., Gladman, B., & McKinnon, W. B. 2015, Icar, 258, 267
Greenstreet, S., Gladman, B., & McKinnon, W. B. 2016, Icar, 274, 366
Greenstreet, S., Gladman, B., McKinnon, W. B., Kavelaars, J. J., & Singer, K. N. 2019, ApJL, 872, L5
Harris, A. W. 1984, in In IAU Colloq. 75: Planetary Rings, ed. R. Greenberg & A. Brahic (Tuscan, AZ: Univ. Arizona Press), 641
Holsapple, K., Giblin, I., Housen, K., Nakamura, A., & Ryan, E. 2002, in Asteroids II, ed. W. F. Bottke, Jr., A. Cellino, P. Paolicchi, & R. P. Binzel (Tucson, AZ: Univ. of Arizona Press), 443
Housen, K. R., & Holsapple, K. A. 1990, Icar, 84, 226
Housen, K. R., & Holsapple, K. A. 2003, Icar, 163, 102
Housen, K. R., & Holsapple, K. A. 2011, Icar, 211, 856
Housen, K. R., Sweet, W. J., & Holsapple, K. A. 2018, Icar, 300, 72
Jewitt, D., & Luu, J. 1993, Natur, 362, 730
Jewitt, D. C., & Luu, J. 2004, Natur, 432, 731
Jewitt, D. C., & Luu, J. X. 1995, AJ, 109, 1867
Jones, R. L., Gladman, B., Petit, J. M., et al. 2006, Icar, 185, 508
Kaib, N. A., Roškar, R., & Quinn, T. 2011, Icar, 215, 491
Kavelaars, J. J., Jones, R. L., Gladman, B. J., et al. 2009, AJ, 137, 4917
Kavelaars, J. J., Lawler, S. M., Bannister, M. T., & Shankman, C. 2020, in The Trans-Neptunian Solar System, ed. D. Prialnik, M. A. Barucci, & L. Young (Amsterdam: Elsevier), 61
Kuchner, M. J., & Stark, C. C. 2010, AJ, 140, 1007
Lawler, S. M., Kavelaars, J. J., Alexandersen, M., et al. 2018a, FrASS, 5, 14
Lawler, S. M., Shankman, C., Kavelaars, J. J., et al. 2018b, AJ, 155, 197
Levison, H. F., & Morbidelli, A. 2003, Natur, 426, 419
Malhotra, R. 1993, Natur, 365, 819
Malhotra, R. 1995, AJ, 110, 420
Melosh, H. J. 1989, Impact Cratering : A Geologic Process (Oxford: Oxford Univ. Press)
Millis, R. L., Buie, M. W., Wasserman, L. H., et al. 2002, AJ, 123, 2083
Nesvorný, D. 2015, AJ, 150, 68
Opik, E. J. 1951, PRIAA, 54, 165
Petit, J. M., Holman, M. J., Gladman, B. J., et al. 2006, MNRAS, 365, 429
Petit, J. M., Kavelaars, J. J., Gladman, B., & Loredo, T. 2008, in The Solar System Beyond Neptune, ed. M. A. Barucci, H. Boehnhardt, D. P. Cruikshank, & A. Morbidelli (Tucson, AZ: Univ. of Arizona Press), 71
Petit, J. M., Kavelaars, J. J., Gladman, B. J., et al. 2011, AJ, 142, 131
Poppe, A. R. 2016, Icar, 264, 369
Schlichting, H. E., Ofek, E. O., Wenz, M., et al. 2009, Natur, 462, 895
Schwamb, M. E., Brown, M. E., Rabinowitz, D. L., & Ragozzine, D. 2010, ApJ, 720, 1691
Schwamb, M. E., Fraser, W. C., Bannister, M. T., et al. 2019, ApJS, 243, 12
Shankman, C., Kavelaars, J., Gladman, B. J., et al. 2016, AJ, 151, 31
Shannon, A., Jackson, A. P., & Wyatt, M. C. 2019, MNRAS, 485, 5511
Singer, K. N., McKinnon, W. B., Gladman, B., et al. 2019, Sci, 363, 955
Spencer, J. R., Stern, S. A., Moore, J. M., et al. 2020, Sci, 367, aay3999
Stern, S. A. 1995, AJ, 110, 856
Szalay, J. R., Poppe, A. R., Agarwal, J., et al. 2018, SSRv, 214, 98
Trujillo, C. A., Jewitt, D. C., & Luu, J. X. 2001, AJ, 122, 457
Tsiganis, K., Gomes, R., Morbidelli, A., & Levison, H. F. 2005, Natur, 435, 459
Van Laerhoven, C., Gladman, B., Volk, K., et al. 2019, AJ, 158, 49
Vitense, C., Krivov, A. V., Kobayashi, H., & Löhne, T. 2012, A&A, 540, A30
Wetherill, G. W. 1967, JGR, 72, 2429
Zahnle, K., Schenk, P., Levison, H., & Dones, L. 2003, Icar, 163, 263